Supplementary Information for

Enhanced Electrocatalytic Reduction of CO_2 via Chemical Coupling between Indium Oxide and Reduced Graphene Oxide

Zhirong Zhang,[†,‖] Fawad Ahmad,[†,‖] Wanghui Zhao,[†,‖] Wensheng Yan,[†] Wenhua Zhang,[*,†] Hongwen Huang,[*,§] Chao Ma,[§] and Jie Zeng[*,†]

[†]Hefei National Laboratory for Physical Sciences at the Microscale, Key Laboratory of Strongly-Coupled Quantum Matter Physics of Chinese Academy of Sciences, Department of Chemical Physics, University of Science and Technology of China, Hefei, Anhui 230026, P. R. China

[§]College of Materials Science and Engineering, Hunan University, Changsha, Hunan, 410082, P. R. China

*To whom correspondence should be addressed.

E-mail: whhzhang@ustc.edu.cn (W. Z.)

E-mail: huanghw@hnu.edu.cn (H. H.)

E-mail: zengj@ustc.edu.cn (J. Z.)

[‖]These authors contributed equally to this work.

Experimental Section

Chemicals and materials. Indium (III) chloride tetrahydrate ($InCl_3 \cdot 4H_2O$), sodium oleate ($C_{18}H_{33}NaO_2$), potassium bicarbonate ($KHCO_3$) and ethanol (C_2H_5OH) were all purchased from Sinopharm Chemical Reagent Co. Ltd (Shanghai, China). GO was purchased from Shanghai Ashine Technology Development Co. Ltd (Shanghai, China). (1-Propanesulfonic acid 3-(trimethylsilyl) sodium salt, DSS) was purchased from Sigma-Aldrich. All the chemicals were used without further purification. Ultrapure Millipore water (18.2 MΩ) was used in all our experiments.

Synthesis of $In(OH)_3$-rGO hybrid. In a typical synthesis, 0.9 mmol of sodium oleate was firstly mixed with 40 mL of preformed GO aqueous suspension (2 mg/mL). After vigorous stirring for 30 min, 0.3 mmol of $InCl_3 \cdot 4H_2O$ was added into the above solution with another 30 min of stirring. Afterwards, the mixture was transferred into a 40 mL Teflon-lined autoclave, sealed and heated at 150 ^oC for 3 h. After naturally cooling down, the product was centrifuged and washed with ethanol three times and dried in vacuum at 45 ^oC overnight for further characterizations.

Synthesis of the In_2O_3-rGO hybrid. In a typical procedure, the as-obtained $In(OH)_3$-rGO hybrid was calcined at 400 ^oC for 5 min in air and then cooled down to room temperature.

Synthesis of $In(OH)_3$ and In_2O_3 nanobelts. The $In(OH)_3$ nanobelts were prepared using the same synthetic procedure as the synthesis of $In(OH)_3$-rGO hybrid except for the absence of GO. The In_2O_3 nanobelts were further obtained by treating the $In(OH)_3$ nanobelts at 400 ^oC for 5 min in air.

Synthesis of In_2O_3/rGO. In the preparation of In_2O_3/rGO, rGO was firstly obtained in the same way as in the synthesis of $In(OH)_3$-rGO hybrid without the addition of $InCl_3 \cdot 4H_2O$. Then 58 wt% of In_2O_3 nanobelts and 42 wt% of rGO were separately dispersed in 10 mL ethanol and stirred for 30 min at room temperature. Then these two solutions were mixed together under magnetic stirring for another 30 min. Afterwards, the mixture was obtained by centrifugation and then dried in vacuum at 45 ^oC.

Electrochemical measurements. All the electrochemical measurements were carried out in an H-cell (separated by Nafion 115 membrane) system. The Pt wire and Ag/AgCl (3 M KCl) electrode were used as the counter electrode and reference electrode, respectively. All potentials were measured against an Ag/AgCl reference electrode and were converted to values with reference to reversible hydrogen electrode (RHE) using E (vs. RHE) = E (vs. Ag/AgCl) + 0.21 V + 0.0591 × pH.

Prior to the electrochemical measurements, the working electrode was prepared. Typically, 5 mg of In_2O_3-rGO hybrid catalyst and 37.5 μL of Nafion solution (5 wt%) were dispersed in 2 mL of ethanol by sonicating for 1 h to form a homogeneous catalyst ink. Then, 320 μL of the catalyst ink was uniformly deposited on carbon papers of 1 cm × 1 cm to act as the working electrode. As a reference, the In_2O_3/rGO and In_2O_3/C catalysts ink were prepared using the similar procedure as that for In_2O_3-rGO hybrid catalyst ink. The linear sweep voltammetry (LSV) was performed in CO_2-saturated and N_2-saturated 0.1 M $KHCO_3$ aqueous solution from 0 V to -1.2 V at a scan rate of 10 mV s^{-1}. The electrochemically active surface area (ECSA) of the working electrodes were estimated according to the equation: ECSA = R_fS, where R_f is the roughness factor, S is the geometric area of the working electrode. The R_f can be determined by the relation $R_f = C_{dl}/60$ μF cm^{-1} based on the double-layer capacitance (C_{dl}) of a smooth oxide surface. C_{dl} was determined by measuring the capacitive current associated with double-layer charging from the scan-rate dependence of cyclic voltammogram (CV). The C_{dl} was estimated by plotting the Δj (j_a-j_c) at 0.75 V against the scan rates, the Δj could be acquired by cyclic voltammetry measurement under the potential windows of 0.7~0.8 V. The electrochemical impedance spectra of the samples were recorded with AC voltage with 5 mV amplitude at -0.7 V within the frequency range from 100 KHz to 100 mHz. Tafel slopes for formate production were calculated from the corresponding current densities at the potential range from -0.48 to -0.55 V and the formate Faradaic efficiency. The electrochemical reduction of CO_2 was carried out in CO_2-saturated 0.1 M $KHCO_3$ electrolyte (pH = 6.8) in the potential range of -0.5 V to -1.2 V at room temperature. After CO_2 was purged into the $KHCO_3$ solution for at least 30 min to remove

residual air in the reservoir, controlled potential electrolysis was conducted at each potential for 45 min. The oxygen generated at the anode was vented out of the reservoir. The gas products of CO_2 electrocatalytic reduction were monitored by an online micro gas chromatography (GC) (GC2014, Shimadzu, Japan) equipped with a TCD detector every 5 min. The durability tests were conducted at the potential of -1.2 V for 10 h. The $KHCO_3$ solution after electrolysis was collected and analyzed on a 400 MHz NMR spectrometer to quantify liquid products.

Calculations details. All the calculations were performed based on density functional theory (DFT) implemented in the VASP package.[1,2] The projector augmented wave method was used to describe the interaction between ions and electrons. The energy cutoff of plane wave basis sets for surface calculations are set as 400 eV. The nonlocal exchange correlation energy was evaluated using the Perdew-Burke-Ernzerhof (PBE) functional.[3] The van der Waals interactions is described using the semi-empirical DFT-D3 type of dispersion energy correction. [4,5] All the atoms were relaxed until the residual forces on all unconstrained atoms were less than 0.02 eV/Å. During frequency calculations, the adsorbates and directly connected In and O atoms were relaxed. $2\times2\times1$ and $2\times3\times1$ k-points grids are used for In_2O_3 (110) unit cell and (2×1) supercell calculations, respectively. HSE06 [6] functional is adopted for the calculation of work function and energy gap, which contains a screening of $\omega = 0.11$ bohr^{-1} to partition the Coulomb potential into short-range (SR) and long-range (LR) terms follows the form:

$$E_{xc}^{HSE}(\omega) = E_x^{HSE,SR} + E_x^{PBE,LR} + E_c^{PBE}$$

where

$$E_{xc}^{HSE,SR} = \frac{1}{4}E_x^{Fock,SR} + \frac{3}{4}E_x^{PBE,SR}$$

The adsorption energies of CO_2 were defined as

$$\Delta E_{ads}(CO_2) = E_{CO_2/In_2O_3} - E_{In_2O_3} - E_{(CO_2)}$$

Where E_{CO_2/In_2O_3}, $E_{In_2O_3}$ and $E_{(CO_2)}$ represent the total energies of the surface slab with the CO_2, the clean surface In_2O_3 (110) slab, and gas phase CO_2, respectively.

The reaction Gibbs free energy of each elementary step was defined as

$\Delta G = \Delta E + \Delta ZPE - T\Delta S$. ΔE is the reaction energy based on density functional calculations and ΔZPE is the energy change of zero point energy correction (*ZPE*). T is temperature and ΔS is the entropy change. Under standard conditions (pH = 0, $p(H_2)$ = 1 bar, U = 0 V vs. SHE at 298.15 K), the Gibbs free energy of H^+ (aq) + e^- equals to that of $\frac{1}{2}H_2$ (g).[7] For adsorbed CO_2^* and $HCOO^{-*}$, the vibrational frequencies of adsorbates were calculated to obtain ZPE contributions according to $ZPE = \sum_i \frac{1}{2} h\upsilon_i$, where υ_i is the frequency and *i* is the frequency number. For gas phase H_2 and CO_2, the values of entropy are obtained from the NIST database at room temperature.[8] And for adsorbed species, only the vibrational entropy (S_v) defined as $S_v = \sum_i R\{\frac{h\upsilon_i}{k_B T}[\exp(\frac{h\upsilon_i}{k_B T}) - 1]^{-1} - \ln[1 - \exp(-\frac{h\upsilon_i}{k_B T})]\}$ are taken into account,[9] where R = 8.314 $J \cdot mol^{-1} \cdot K^{-1}$, T = 298.15 K, h = $6.63*10^{-34} J \cdot S$, $k_B = 1.38*10^{-23} J \cdot K^{-1}$.

For the composition of rGO and In_2O_3(110) nanosheet, the charge transfer direction can be evaluated by the alignment of the band structures of rGO and In_2O_3(110). Based on HSE06 calculations, the band gap and the work function of In_2O_3(110) are calculated as 2.10 eV and 6.38 eV, respectively, which agree well with previous theoretical work.[10] According to the theoretical calculation of Priyank V. Kumar et al, the work function range of rGO with epoxy group is 4.35-5.60 eV.[11] In our work, The work function of rGO with different epoxy group coverages are also calculated as listed in Table S1. The work function of rGO increases with the oxygen coverage, and the work function of perfect graphene is 4.54 eV. So the electron will spontaneously run from rGO to In_2O_3 (110), as shown in Figure S15.

Instrumentation. TEM images were taken using a Hitachi H-7650 transmission electron microscope at an acceleration voltage of 100 kV. HRTEM and HAADF-STEM were carried out on a JEOL ARM-200F field-emission transmission electron microscope operating at 200 kV accelerating voltage. XRD patterns were recorded by using a Philips X'Pert Pro Super diffractometer with Cu-Kα radiation (λ = 1.54178 Å). Raman spectra were detected by a Renishaw RM3000 Micro-Raman system with a 514.5 nm Ar laser. The mass content of In_2O_3 in In_2O_3/rGO hybrid was determined by ICP-AES (Atom scan Advantage, Thermo Jarrell Ash, USA). XPS measurements were carried out on a VG ESCALAB MK II X-ray photoelectron

spectrometer with an exciting source of Mg Kα = 1253.6 eV. The binding energies obtained in the XPS spectral analysis were corrected for specimen charging by referencing C 1s to 284.6 eV. The liquid products were quantified by nuclear magnetic resonance (Bruker AVANCE AV III 400) spectroscopy. XANES spectra (C *K*-edge, and In M_2-edge) were measured at the beamline 12B of national synchrotron radiation laboratory (NSRL, Hefei).

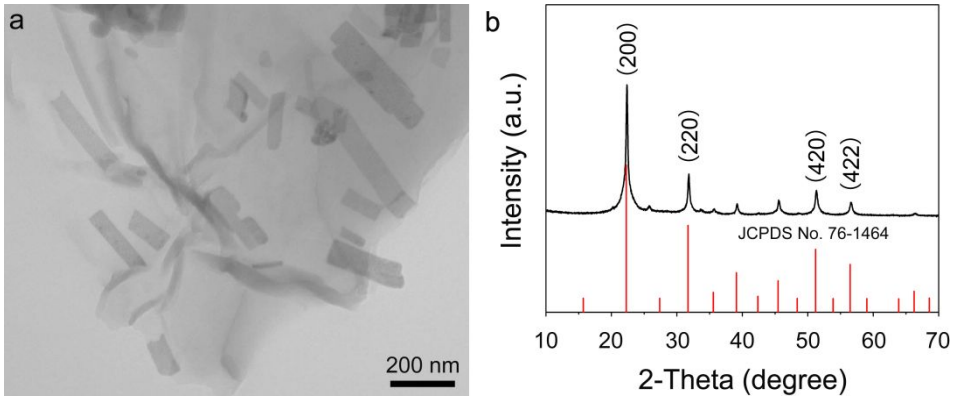

Figure S1. (a) TEM image and (b) XRD pattern of the $In(OH)_3$ nanobelts-rGO hybrid.

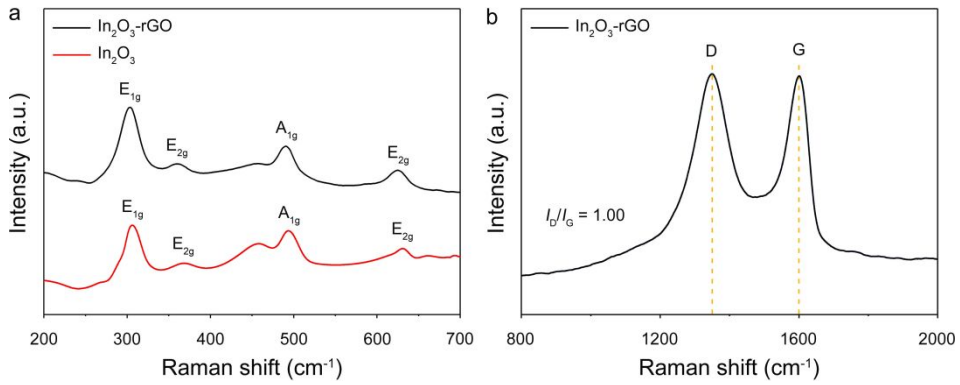

Figure S2. (a) Raman spectra of In_2O_3 in In_2O_3-rGO hybrid and porous In_2O_3 nanobelts. (b) Raman spectra of rGO in In_2O_3-rGO hybrid.

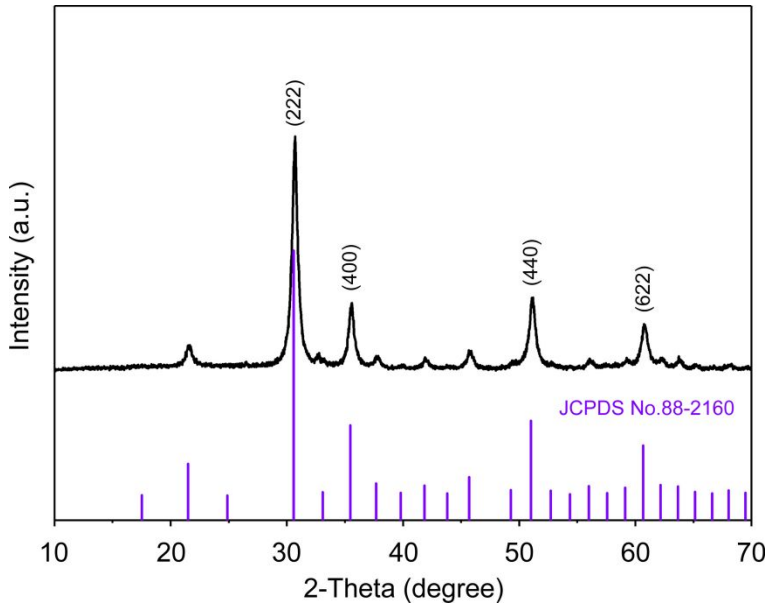

Figure S3. XRD pattern of the In_2O_3-rGO hybrid.

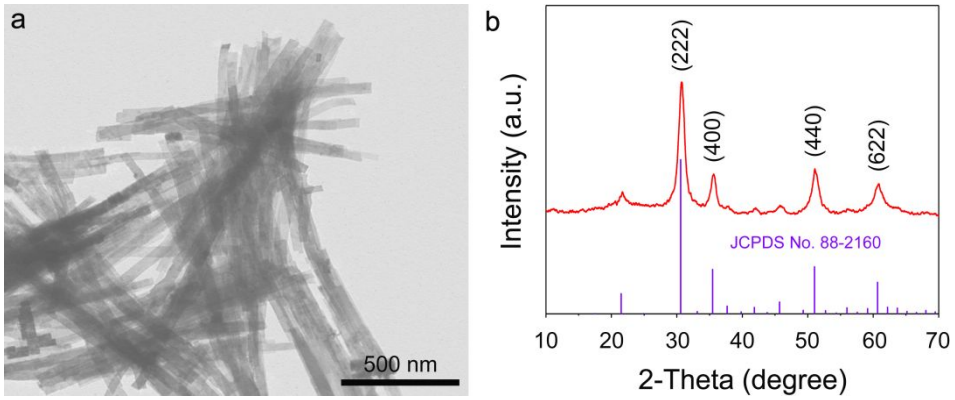

Figure S4. (a) TEM image and (b) XRD pattern of the porous In_2O_3 nanobelts.

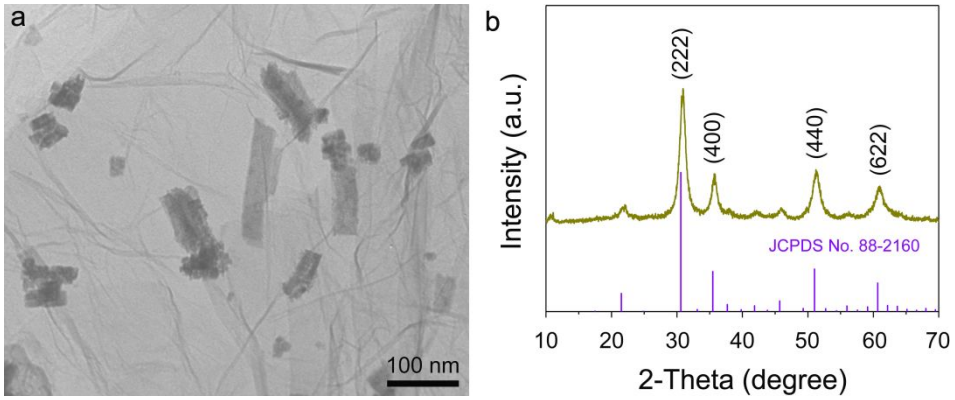

Figure S5. (a) TEM image and (b) XRD pattern of the In_2O_3/rGO.

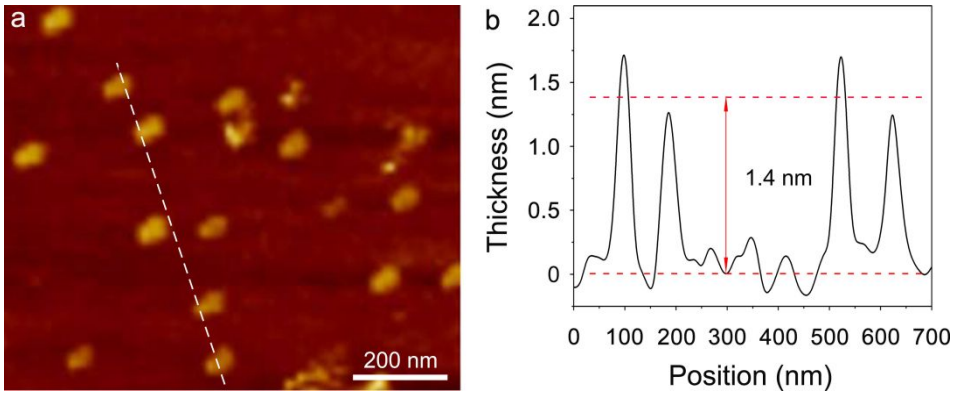

Figure S6. (a) AFM image of the porous In_2O_3 nanobelts and (b) the corresponding height profile along the direction marked by white line.

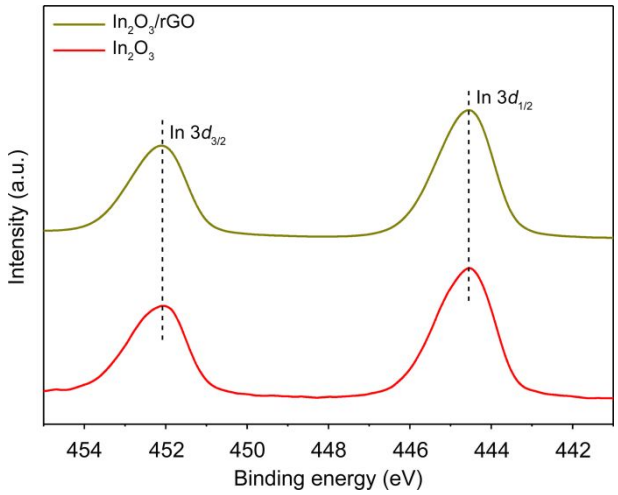

Figure S7. In 3*d* XPS spectra of In_2O_3/rGO and In_2O_3 nanobelts.

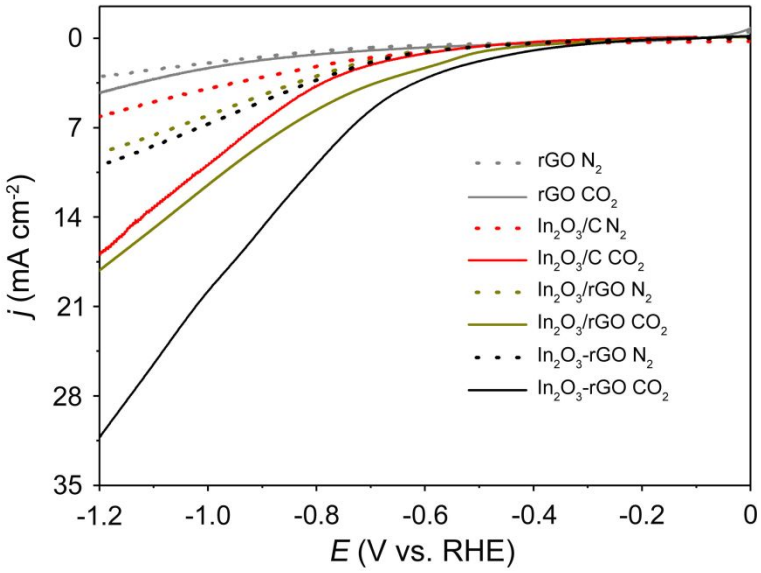

Figure S8. Linear sweep voltammetry (LSV) curves for different catalysts in a CO_2-saturated (solid line) and N_2-saturated (dashed line) 0.1 M $KHCO_3$ aqueous solution at a scan rate of 10 mV s^{-1}.

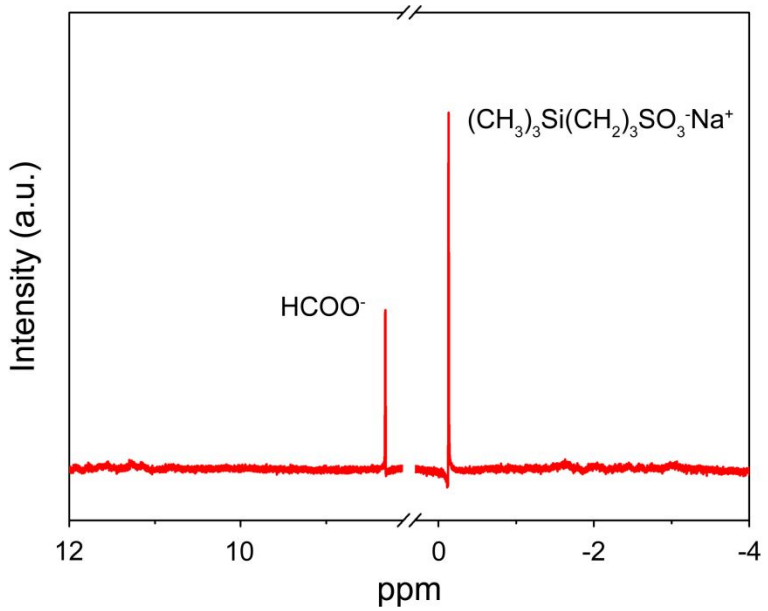

Figure S9. ^{1}H NMR spectra for liquid phase product characterization. Representative ^{1}H NMR spectra of the electrolyte after electrolysis at -0.8 V (vs. RHE) for In_2O_3-rGO hybrid catalyst in CO_2-saturated 0.1 M $KHCO_3$ electrolyte. DSS is used as an internal standard for calibration and liquid phase product identification and quantification.

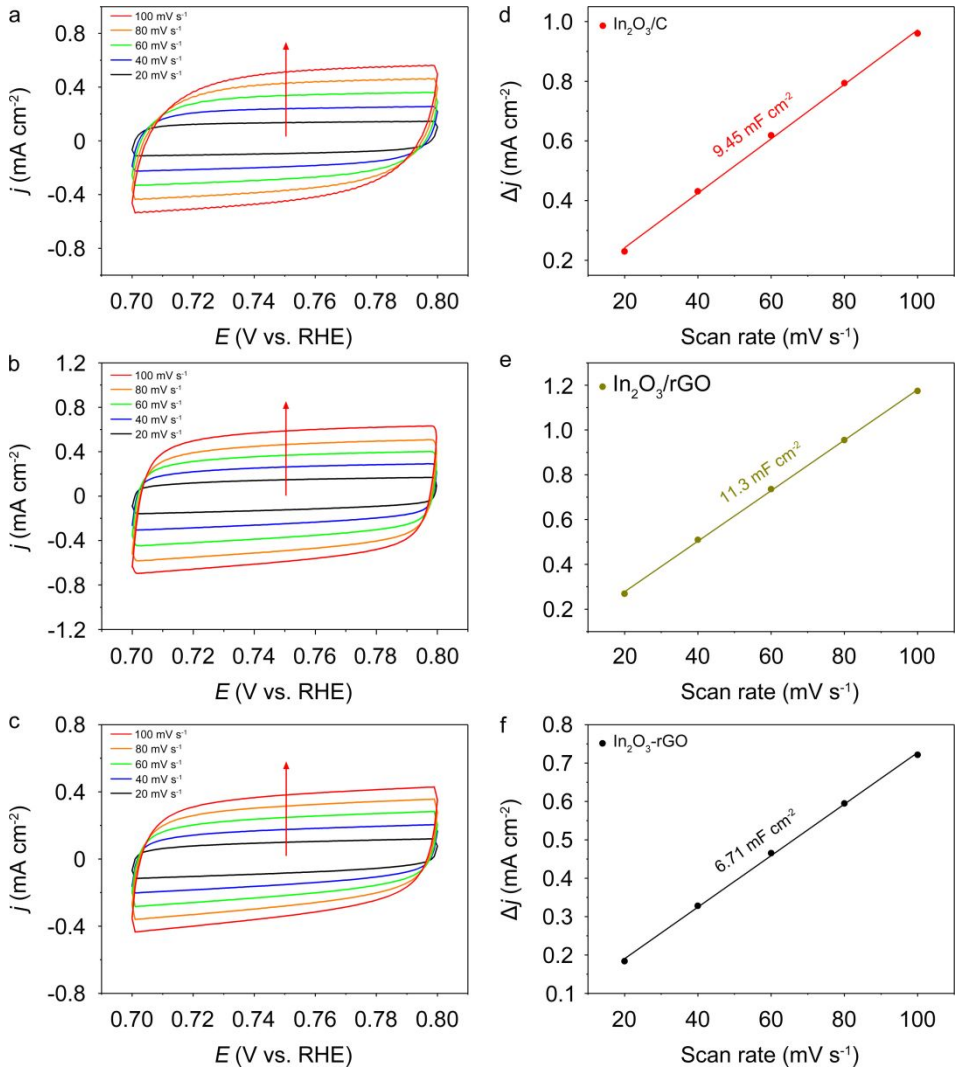

Figure S10. CVs of (a) In_2O_3/C, (b) In_2O_3/rGO and (c) In_2O_3-rGO hybrid catalysts measured in N_2-saturated 0.1 M $KHCO_3$ aqueous solution at scan rates from 20 to 100 mV s^{-1}, respectively. Charging current density differences plotted against scan rates for (d) In_2O_3/C, (e) In_2O_3/rGO and (f) In_2O_3-rGO hybrid catalysts.

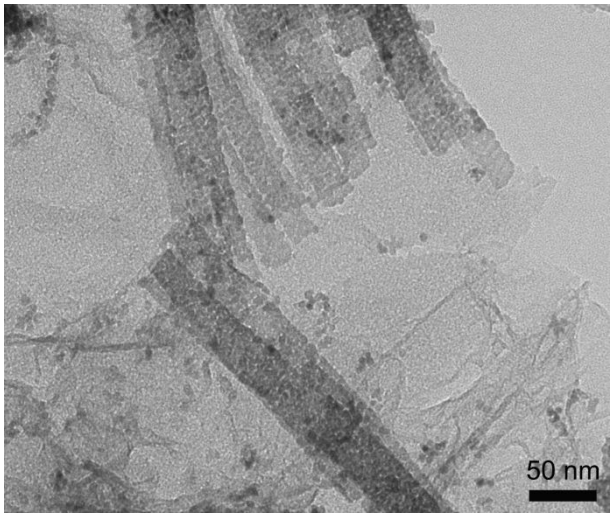

Figure S11. TEM image of In_2O_3-rGO hybrid after the electrochemical tests.

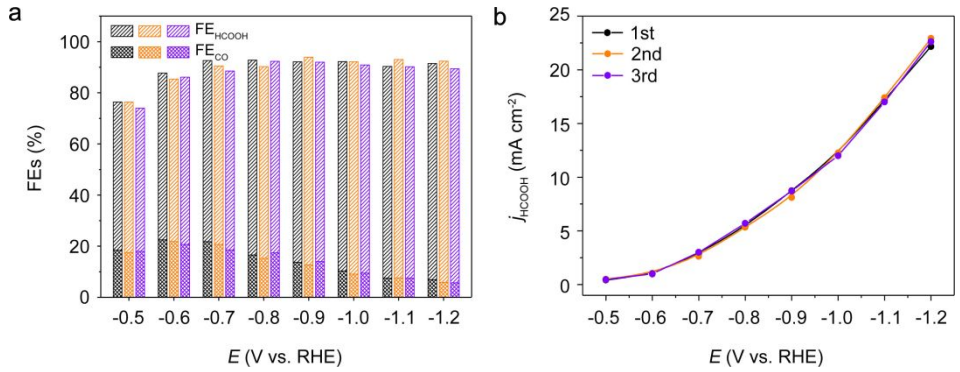

Figure S12. (a) Faradaic efficiencies and (b) current densities at different voltages using the same In_2O_3-rGO catalyst for three times. The black, orange, and purple column represents the FEs of the first, second, and third time, respectively.

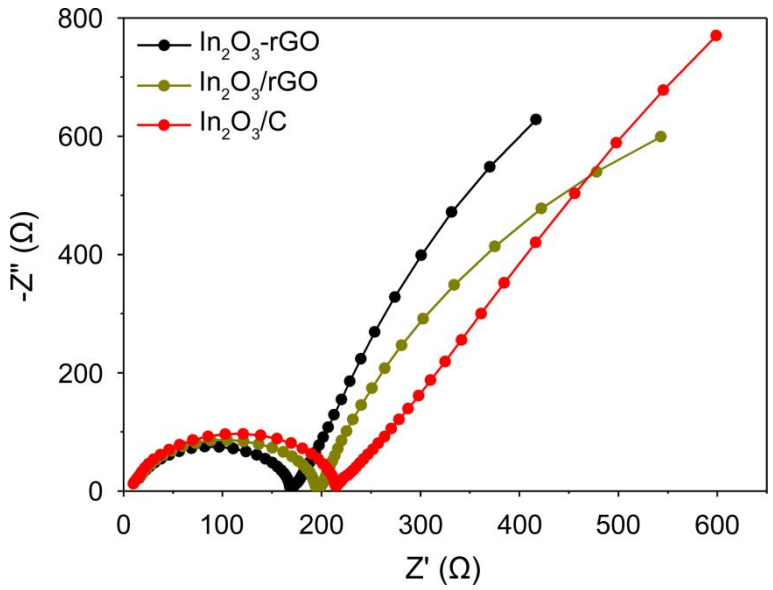

Figure S13. Electrochemical impedance spectra for the In_2O_3-rGO hybrid, In_2O_3/rGO and In_2O_3/C catalysts.

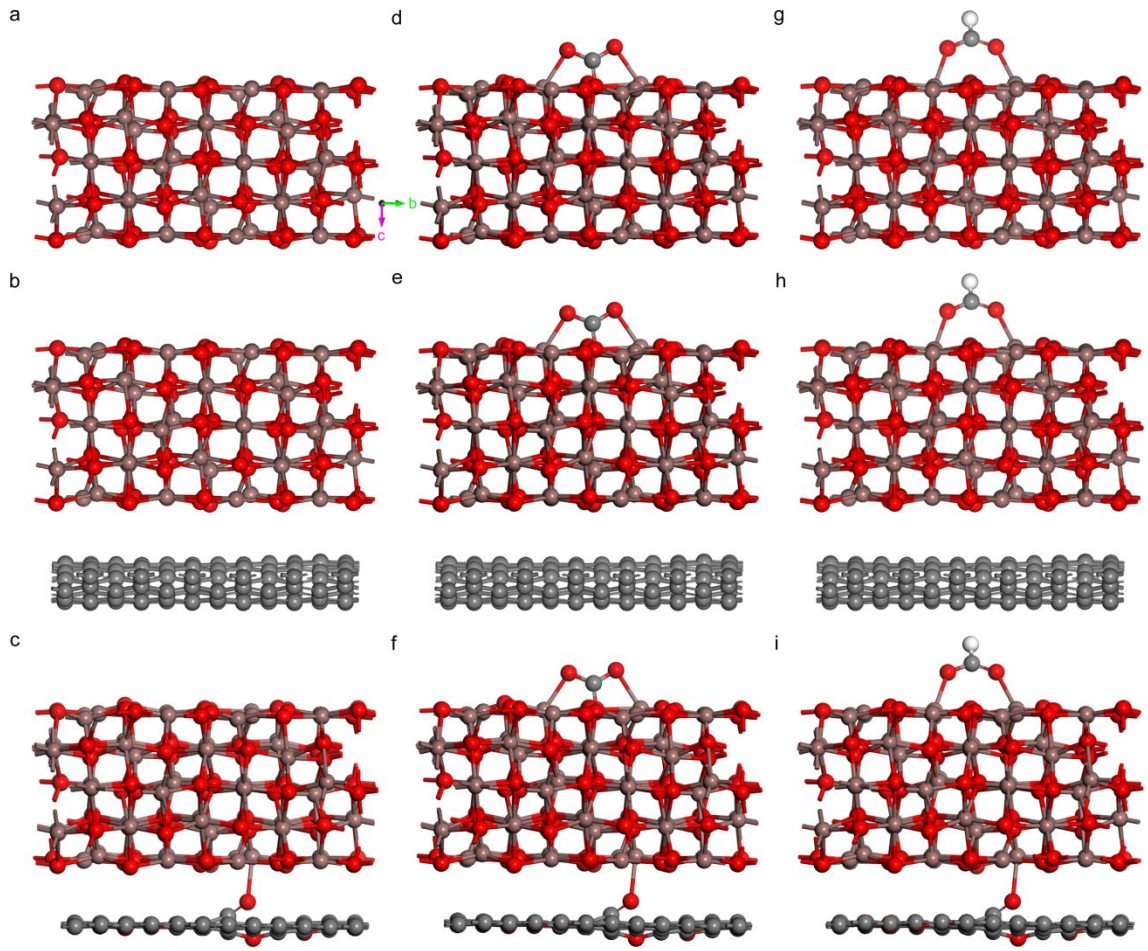

Figure S14. (a-c) Crystal structure model of cubic In_2O_3, In_2O_3/rGO, and In_2O_3-rGO hybrid with top view of (110) plane, respectively. (d-f) Configuration of CO_2 adsorption on (110) plane of cubic In_2O_3, In_2O_3/rGO, and In_2O_3-rGO hybrid, respectively. (g-i) Configuration of $HCOO^-$* adsorption on (110) plane of cubic In_2O_3, In_2O_3/rGO, and In_2O_3-rGO hybrid, respectively. In, O, C, and H atoms are depicted as brown, red, gray, and white spheres, respectively.

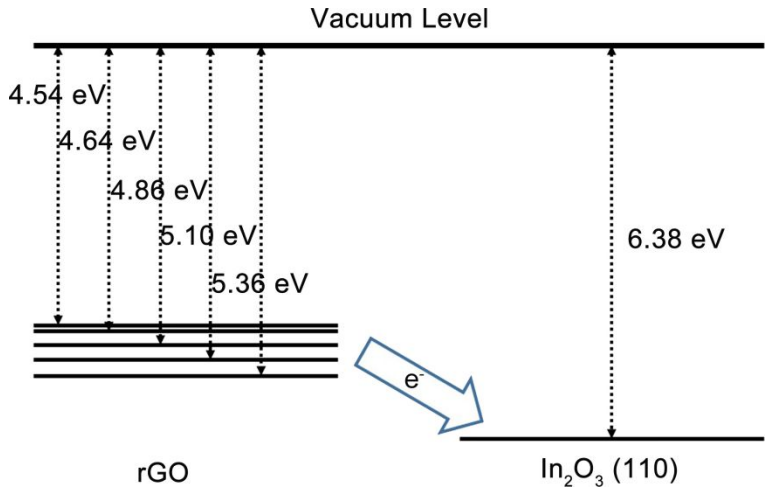

Figure S15. The work function of rGO and In_2O_3 (110).

Table S1. The work functions of different oxygen coverage of rGO.

O coverage (%)	0	2	4	6	20
Work function (eV)	4.54	4.65	4.86	5.10	5.36

1. Supplementary Table

Table S2. Comparison of the electrocatalytic performance for reducing CO_2 to formate on different electrodes and electrolytes.

Catalyst	Electrolyte	E_{app} (V)	j_{HCOOH} (mA cm^{-2})	$FE_{formate}$ (%)	Ref.
Sn/SnOx	0.5 M $NaHCO_3$	-0.7 V vs. RHE	1.04	58	12
SnOx/carbon black	0.1 M $NaHCO_3$	-1.16 V vs. RHE	4.644	86	13
Sn-pNWs	0.1 M $KHCO_3$	-0.8 V vs. RHE	4.806	80.1	14
Sn-graphene	0.1M $NaHCO_3$	-1.16 V vs. RHE	18.78	89	15
$Sn_6O_4(OH)_4$	0.1 M K_2SO_4	-0.8 V vs. RHE	0.72	60	16
$Cu_{57}Sn_{43}$	0.5 M $KHCO_3$	-0.92 V vs. RHE	1.42	57	17
$Ag_{76}Sn_{24}$	0.5 M $NaHCO_3$	-0.8 V vs. RHE	15.6	80	18
CoO_x	0.1 M Na_2SO_4	-0.25 V vs. RHE	9.0	90	19
Polycrystalline Sn	0.1 M $KHCO_3$	-1.08 V vs. RHE	4.42	88.4	20
Dendritic $Cu_{0.2}In_{0.8}$	0.1 M $KHCO_3$	-1.0 V vs. RHE	0.73	62	21
Co_3O_4	0.1 M $KHCO_3$	-0.88 V vs. SCE	0.44	64.3	22
Boron–doped graphene	0.1 M $KHCO_3$	-1.4 V vs. SCE	0.99	66	23
In_2O_3/C	**0.1 M $KHCO_3$**	**-1.2 V vs. RHE**	**6.95**	**48.2**	**This Work**
In_2O_3-rGO	**0.1 M $KHCO_3$**	**-1.2V vs. RHE**	**22.17**	**84.6**	**This Work**

REFERENCES

(1) Kresse, G.; Hafner, J. *Phys. Rev. B* **1993**, *47*, 558-561.

(2) Kresse, G.; Furthmüller, J.; *Phys. Rev. B: Condens. Matter Mater. Phys.* **1996**, *54*, 11169-11186.

(3) Perdew, J. P.; Burke, K.; Ernzerhof, M.; *Phys. Rev. Lett.* **1996**, *77*, 3865-3868.

(4) Grimme, S.; Antony, J.; Ehrlich, S.; Krieg, H. *J. Chem. Phys.* **2010**, *132*, 154104.

(5) Grimme,S.; Ehrlich, S.; Goerigk, L.; *J. Comput. Chem.* **2011**, *32*, 1456-1465.

(6) Heyd, J.; Scuseria, G. E.; Ernzerhof, M. *J. Chem. Phys.* **2003**, *118*, 8207-8215.

(7) Nørskov, J. K.; Rossmeisl, J.; Logadottir, A.; Lindqvist, L.; Kitchin, J. R.; Bligaard, T.; Jónsson, H. *J. Phys. Chem. B* **2004**, *108*, 17886-17892.

(8) Computational Chemistry Comparison and Benchmark Database. http://cccbdb.nist.gov/

(9) Howalt, J. G.; Bligaard, T.; Rossmeisl, J.; Vegge, T. *Phys. Chem. Chem. Phys.* **2013**, *15*, 7785-7795.

(10) Walsh, A.; Catlow, C. R. A. *J. Mater. Chem.* **2010**, *20*, 10438-10444.

(11) Kumar, P. V.; Bernardi, M. J.; Grossman, C. *ACS nano*, **2013**, *7*, 1638-1645.

(12) Chen, Y.; Kanan, M. W. *J. Am. Chem. Soc.* **2012**, *134*, 1986-1989.

(13) Zhang, S.; Kang, P.; Meyer, T. J. *J. Am. Chem. Soc.* **2014**, *136*, 1734-1737.

(14) Kumar, B.; Atla, V.; Brian, J. P.; Kumari, S.; Nguyen, T. Q.; Sunkara, M.; Spurgeon, J. M. *Angew. Chem. Int. Ed*. **2017**, *56*, 3645-3649.

(15) Lei, F.; Liu, W.; Sun, Y.; Xu, J.; Liu, K.; Liang, L.; Yao, T.; Pan, B.; Wei, S.; Xie, Y. *Nat. Commun.* **2016**, *7*, 12697.

(16) Baruch, M. F.; Pander, J. E.; White, J. L.; Bocarsly, A. B. *ACS Catalysis* **2015**, *5*, 3148-3156.

(17) Watanabe, M.; Shibata, M.; Kato, A.; Azuma, M.; Sakata, T. *J. Electrochem. Soc.* **1991**, *138*, 3382-3389.

(18) Luc, W.; Collins, C.; Wang, S.; Xin, H.; He, K.; Kang, Y.; Jiao, F. *J. Am. Chem. Soc.* **2017**, *139*, 1885-1893.

(19) Gao, S.; Lin, Y.; Jiao, X.; Sun, Y.; Luo, Q.; Zhang, W.; Li, D.; Yang, J.; Xie, Y. *Nature* **2016**, *529*, 68-71.

(20) Hori, Y.; Wakebe, H.; Tsukamoto, T.; Koga, O. *Electrochim. Acta* **1994**, *39*, 1833-1839.

(21) Hoffman, Z. B.; Gray, T. S.; Moraveck, K. B.; Gunnoe, T. B.; Zangari, G. *ACS Catalysis* **2017**, *7*, 5381-5390.

(22) Gao, S.; Jiao, X.; Sun, Z.; Zhang, W.; Sun, Y.; Wanng, C.; Hu, Q.; Zu, X.; Yang, F.; Yang, S.; Liang, L.; Wu, J.; Xie, Y. *Angew. Chem. Int. Ed.* **2016**, *55*, 698-702.

(23) Narayanaru, S.; Mohammed, A. N.; Thazhe, V. V.; Krishnamurty, S.; Phani, K. L. *Chem. Commun.* **2015**, *51*, 16061.